Numerical and Experimental Flow Analysis of Moving Airfoils with Laminar Separation Bubbles

Rolf Radespiel,* Jan Windte,† and Ulrich Scholz‡
Technical University of Brunswick, 38106 Brunswick, Germany

Experimental measurements and unsteady Reynolds-averaged Navier–Stokes simulations of the low-Reynolds-number flow past an SD7003 airfoil with and without plunge motion at $Re = 60$ k are presented, where transition takes place across laminar separation bubbles. The experimental data consist of high-resolution, phase-locked particle image velocimetry measurements in a wind tunnel and a water tunnel. The numerical simulation approach includes transition prediction which is based on linear stability analysis applied to unsteady mean-flow data. The numerical results obtained for steady onflow are validated against particle image velocimetry data and published force measurements. Good agreement is obtained for specific turbulence models. Flows with plunge motion reveal strong effects of flow unsteadiness on transition and the resulting laminar separation bubbles which are well captured in the simulations.

Nomenclature

A	=	amplitude of oscillation
c	=	airfoil chord
c_l	=	lift coefficient
c_{df}	=	friction drag coefficient
c_{dp}	=	pressure drag coefficient
f	=	frequency of airfoil motion
N	=	N factor
n	=	amplitude exponent of single wave mode
p	=	pressure
Tu	=	turbulence intensity
t	=	time
U_e	=	total velocity at boundary-layer edge
U_∞	=	freestream velocity
u, v, w	=	velocity components
v_g	=	group velocity of single wave mode
x, y, z	=	local cartesian coordinates of stability analysis in streamwise, spanwise and normal directions
α	=	complex wave number in x-direction, angle of attack
β	=	complex wave number in y direction
ζ	=	effective angle of attack for airfoil motion
κ	=	ratio of specific heats
μ_t	=	turbulent viscosity
ρ	=	density
$\rho \overline{u'v'}$	=	turbulent shear stress
ω	=	complex frequency of wave mode

Superscripts

$\tilde{}$	=	superscript denoting ensemble averages of the unsteady Reynolds-averaged Navier–Stokes solution
$\bar{}$	=	superscript denoting time averages

*Professor, Head of the Institute, Institute of Fluid Mechanics; r.radespiel@tu-braunschweig.de. AIAA Senior Member.

†Research Scientist, Institute of Fluid Mechanics; j.windte@ tu-braunschweig.de.

‡Research Scientist, Institute of Fluid Mechanics; u.scholz@ tu-braunschweig.de.

I. Introduction

THE aerodynamics of low-speed low-Reynolds-number flows over airfoils and wings has been studied for decades in experimental and numerical works. For designing model airplanes with fixed wings, a rich experimental data base grew over the years. Here, the pioneering work of F. Schmitz [1] is mentioned, and much work was later performed by researchers at Stuttgart University, Germany [2,3]. More recently, M. Selig and coworkers developed advanced aerodynamic design methodologies for airfoils and performed a large amount of measurements [4,5]. The subject of low-Reynolds-number flows does receive more attention presently as advances in the field of microsystem technologies enable the development of micro aerial vehicles (MAVs) with a broad variety of applications. Some of the MAV concepts consider flapping wing propulsion with strong unsteady flow effects. Here, published work focuses on inviscid flow analysis of airfoil and wing motion [6,7], and analysis of purely laminar or fully turbulent flows [8,9] and corresponding experiments. Not much has been published about the flow phenomenology and simulation methodology of moving airfoils and wings that include the transition of laminar to turbulent boundary layers.

Recently developed MAVs with masses on the order of 100 g, i.e., the "Black Widow" [10], have Reynolds numbers of about $Re = 50–200$ k. Important for this flight regime is that transition usually occurs in combination with a large laminar separation bubble (LSB). The LSB is a flow in which a laminar separation takes place that is in most cases caused by an adverse pressure gradient along the smooth aerodynamic surface. Small disturbances present in the laminar flow are strongly amplified in the shear layer of the separated flow and rapid transition to turbulence takes place. The turbulence, in turn, creates a large momentum transport normal to the shear layer so that the flow reattaches to the surface and a closed bubble is formed in the time-averaged mean. Laminar separation bubbles can have large, adverse aerodynamic effects. Usually, they create additional drag as they displace the outer, inviscid flow. This results in reduced suction over the forward portion of airfoils and wings and decreases pressure recovery in rear parts, so the additional drag is mostly pressure drag. The increase of pressure drag depends on the size of the LSB, in particular on its thickness in the normal-wall direction. A more dramatic effect occurs if the transition process in the separated shear layer is relatively slow and the adverse pressure gradient is strong. Then turbulent momentum transport is not sufficient to close the bubble and a large separation occurs that extends right to the trailing edge. This causes a sudden loss of lift and a strong increase of drag along with significant hysteresis effects of force coefficients with varying angle of attack. Note that the break up of LSBs may be experienced over a broad range of Reynolds numbers.

The transition process from laminar to turbulent boundary layers for flows with LSBs usually starts well upstream of the laminar separation. In the first stage of the transition process, external broadband disturbances due to freestream turbulence or acoustic waves, generate small, harmonic waves within the laminar boundary layer upstream of the separation. These unstable waves grow exponentially while traveling downstream. This linear process constitutes the second stage of transition. For the low-disturbance environment investigated in this paper, according to the research of Würz [11], Lang et al. [12], and Marxen et al. [13], the primary instability mechanism encountered in this stage is initially of the Tollmien–Schlichting (TS) type, and remains dominated by this type up into the separated flow region. There, a smooth shift over to the Kelvin–Helmholtz (KH) instability may take place, which can become dominant in the rear part of the second stage [14]. This stage extends across a large portion of the flow compared with the third stage of transition, in which the distortions become so large that saturation occurs and secondary instabilities can grow on the distorted boundary-layer flow; this behavior is characterized with nonlinear interactions. Finally, the number of spatial and temporal modes grows rapidly and the ordered laminar structures break down into turbulence.

Although direct numerical flow simulations serve well for basic flow research on transition flow phenomena, there is the need for computationally efficient simulation methods that can be used within aerodynamic design cycles. Aerodynamic design and analysis tools mostly in present use for flows with laminar separation bubbles are based on interacting boundary-layer theory [15] and they are restricted to two-dimensional steady flows. Recent work has therefore addressed the feasibility of coupling Reynolds-averaged Navier–Stokes (RANS) solvers with suitable means for transition prediction to simulate low-Reynolds-number flows with laminar separation bubbles. Detailed comparisons with experimental data and large-eddy simulations (LES) indicate that the choice of the turbulence model plays an important role in the mutual success of this approach [16,17].

The present paper reviews the progress made so far and presents an extension of the RANS-based simulation methodology to unsteady flows with airfoil motion in which both the mean-flow boundary layers and the transition process exhibit unsteady effects. This engineering approach is expected to complement the existing approximate methods in the near future. The goal of the presented work is to achieve accurate engineering solutions for unsteady low-Reynolds-number flows including LSBs in the ensemble-averaged mean. Even though this paper addresses the case of the steady and unsteady flows over airfoils, the approach can be extended to three-dimensional flows as well. These three-dimensional flows could be three-dimensional wing flows or three-dimensional flows over bodies where transition can be correlated to the linear stability behavior of Tollmien–Schlichting and crossflow waves and amplification factors can be integrated along trajectories of the group velocity associated with these waves.

II. Numerical Simulation Methods

A. Simulation Approach

The simulation approach addresses the computation of low-Reynolds-number flows with laminar separation bubbles using the unsteady Reynolds-averaged Navier–Stokes (URANS) equations. Transition location along the airfoil is estimated by using the results of stability analysis of the second stage in the preceding described transition process. Stability analysis is performed by directly investigating the velocity profiles from the RANS-solution with a solver for the linear stability equations (LST). In contrast to approaches in which only the pressure distribution is transferred to combined boundary-layer and LST solvers, this has the advantage that the analysis can be performed in the separated region of LSBs and for unsteady flows where traditional boundary-layer methods cannot be applied. No matter if the waves in this stage are amplified by a viscous (TS) or inviscid (KH) instability mechanism, both types are covered by the stability analysis [14]. The amplification rates of

the primary instabilities in this stage computed by LST compare very well with the rates predicted by well-resolved direct numerical simulation (DNS) [14,18]. Using the e^N method [19] the calculated amplification rates are integrated to N factor envelopes and used to predict the transition location by comparison to a critical N factor. As the receptivity mechanism in the first stage of the transition process cannot be modeled with linear stability analysis, it has to be taken into account by an empirical calibration of the critical N factor to be used with this method. The third stage of the transition process is neglected. As this stage is rather short, there is only a rather small difference in the location of the end of the second stage and the breakdown to turbulence. This difference is taken into account by the choice of an empirical critical N factor, which basically means that an extrapolation of the linear amplifications is performed.

There is some similarity of the present approach with previous work of Stock and Haase [20,21]. However, whereas those authors use an intermittency function to describe the transitional growth of turbulence from laminar to fully turbulent flowfields, we assume that the selected turbulence model will predict the gradual growth of turbulence. Upstream of the location of critical N factor the flow is assumed as laminar. This is modeled by setting the source terms of the transport equations of turbulence to zero. Then, following the computation of the transition point, the original production terms of the applied turbulence model are activated in the flowfield downstream of the surface normal associated with the surface transition location. Hence, we use nonlocal data to define the source terms of the turbulence equations, however, this is not an uncommon practice for the turbulence models considered in the present work. This numerical treatment of transition in the turbulence models allows smooth growth of turbulence quantities until a fully turbulent boundary layer is obtained. Hence, the total rate of change of turbulence, i.e., temporal and spatial change, is taken into account which is necessary to model unsteady flows. Secondly, we introduce a novel formulation of the e^N method that takes into account the temporal development of disturbances within the unsteady boundary-layer flow state.

B. Navier–Stokes Code Flower

The numerical results are obtained using the code FLOWer [22]. The Navier–Stokes solver FLOWer uses a block-structured computational domain around the aerodynamic configuration. The flow equations are discretized based on the finite-volume approach, either with the cell-vertex or the cell-centered formulations. Various options are implemented for treating the convective fluxes. These are central schemes with scalar or matrix-valued dissipation, and upwind schemes as well. Integration in time is performed by explicit multistage schemes. Implicit residual averaging, multigrid, and local time steps improve convergence for steady-state flow computations. Time-accurate computations are realized by using the dual time-stepping approach. Airfoil motion is taken into account by moving the complete coordinate mesh. Both convergence and accuracy of low-speed flow simulations are enhanced by a preconditioning technique. The code is optimized for vector computers. Parallel computations are based upon message passing interface (MPI) and the use of a high-level communication library. A number of turbulence models are implemented in the code. These include algebraic eddy-viscosity models, one- and two-equation models, algebraic stress and Reynolds stress models [23].

C. Linear Stability Equations Solver Coast3

The numerical method used for determining local amplification of disturbances is more general compared with the stability theory based on the Orr–Sommerfeld equation. Coast3 [24] treats laminar, compressible boundary layers. The boundary layer is assumed to be a parallel flow. The harmonic wave assumption is applied to the variables u, v, w, p, T

$$q = \tilde{q}(x, y, z, t) + q'(x, y, z, t), \qquad q'(x, y, z, t) = \hat{q}e^{i(\alpha x + \beta y - \omega t)}$$

Here, the quantity q is decomposed into the basic state of the boundary layer $\tilde{q}$, which is slowly changing with time, and the single

wave mode q'. Assuming that the frequency of the single wave mode is much larger than the frequencies in the temporal distribution of the basic flow state, the time dependence of the evolution matrices of the system of five stability equations can be neglected and the stability problem solved at a discrete time is approximately the same as for stationary basic flow states. Coast3 solves the linear eigenvalue problem for the complex eigenvalue ω, where the real wave numbers α and β (for three-dimensional cases) are prescribed by the user. Hence, the temporal stability problem is solved. The system of differential equations is discretized with symmetrical second-order differences. This yields a $5n$-dimensional complex band matrix where n is the number of grid points in the wall-normal direction. The numerical eigenvalue computation is accomplished with a generalized inverse Rayleigh iteration [25] which takes into account the banded structure of the algebraic problem. The code provides efficient searching strategies that can be used to find the range of unstable modes for a given flow problem. A data base method to find the range of amplified spanwise wave numbers is offered as well. An option for boundary-layer computations for a given pressure distribution is also available.

D. Transition Prediction for Unsteady Flow

A quite successful method for transition predictions was derived from observations, that the location of the final transition phase (breakdown) is in many cases dominated by the behavior of the primary instabilities with exponential growth. It was found that the point where the boundary layer becomes fully turbulent correlates well with a certain amplification factor of the most unstable primary wave, which is calculated from the point of neutral stability up to the location with fully turbulent flow. These findings constitute the so called e^N method [19].

The assumptions needed to apply the method to the problem of predicting transition of LSBs state that initial and external disturbances of the laminar boundary layer are small. This concerns the surface roughness, external turbulence, acoustic disturbances, noise, and probably others. Second, the laminar boundary layer must be thin and grow slowly with x, to approximate parallel flow. Further, the location of the final transition phase (breakdown) must depend mainly on the behavior of primary instable waves. The second assumption may appear questionable, at first sight. However, extensive numerical experience from numerical stability computations and comparisons with the results of DNS by Lang et al. [12] and Marxen et al. [13] indicate that the assumption of parallel flow needed for the linear stability computations is sufficiently satisfied for a broad range of LSBs. That is, the growth rates of primary instabilities computed by linear stability theory compare very well with the rates predicted by well-resolved DNS [14,18].

A suitable mathematical formulation of the e^N method may be obtained from kinematic wave theory [26]. Here, only the two-dimensional incompressible flows are considered where two-dimensional waves traveling in the x-direction exhibit maximum amplification, according to Squire's Theorem. By assuming the existence of a differentiable phase function, $\theta = \alpha x - \beta t$, of the wave mode and the existence of a dispersion relation, $\omega = \Omega(\alpha, x, y, t)$, the real part of the group velocity which represents the energy propagation of the wave is obtained as the gradient

$$v_g = \frac{\partial \omega_r}{\partial \alpha_r}$$

The group velocity can be used to define material derivatives of quantities that propagate along with the wave [26]. It is found that the wave number and the frequency remain constant in a homogeneous shear flow without gradients in x direction. For stationary basic flow states that vary with x, the frequency of the wave is constant but the wave number varies. For transition analysis of stationary two-dimensional boundary layers over airfoils it is then straightforward to consider the overall amplification factor $A(x)/A_0$ of the perturbation amplitude with reference to the amplitude at the neutral point A_0 for a fixed frequency. This is obtained by integration of the local spatial

amplification rates α_i:

$$\frac{A(x)}{A_0} = e^{\int_{x_o}^{x} -\alpha_i \, dx}$$

The so called N factor is then obtained by taking the maximum value of the amplitude exponent for all unstable modes

$$N(x) = \max_{\omega} \left[\int_{x_0}^{x} -\alpha_i(x, \omega) \, dx \right]$$

which forms an envelope over the investigated modes. The point where the local N factor exceeds the critical value determines the location of breakdown to turbulence as discussed earlier. The solution of the temporal stability problem is often preferable to the spatial problem. One can transform temporal growth into spatial growth by using the Gaster transformation [27]:

$$\alpha_i = -\omega_i / v_g$$

This relation is obtained by assuming small amplification rates. However, it is common to use it for integrating spatial distributions of amplitude ratios from the results of efficient temporal stability solvers in boundary layers of airfoils and wings with significant amplification rates. Its applicability for the present flows with laminar separation bubbles will be discussed in the results section. Using this relation and computing the change of the exponent Δn of the amplitude ratio over a certain distance Δx, one obtains

$$\Delta n = \int_{x}^{x+\Delta x} \frac{\omega_i}{v_g} \, dx$$

With $dx = v_g dt$ this becomes a time-stepping scheme for the change of n with time

$$\Delta n = \ln \frac{A(x + v_g \Delta t)}{A(x)} = \int_{t}^{t+\Delta t} \omega_i(x) \, dt$$
$$n(x + v_g \Delta t) = n(x) + \Delta n$$

Then, the new values of n at the position $x + v_g \Delta t$ may be interpolated to any position x, for examples to positions of grid points. Obviously, this scheme can be used to compute spatially varying amplitude exponents for unsteady basic flow states. However, it should be noted that for unsteady basic flows, the kinematics of waves states that the material derivative of the frequency is

$$\frac{D}{Dt} \omega_r = \frac{\partial}{\partial t} \omega_r + v_g \frac{\partial}{\partial x} \omega_r = \Omega_t$$

A wave propagating with the group velocity therefore changes its frequency. This indicates that an e^N method for unsteady basic flows should select temporal growth rates that correspond to theses changes in frequency, when integrating amplitude ratios and the N factor. At this point, our present numerical implementation assumes that these variations of frequencies along the group velocity trajectory can be neglected and the N factor is assembled as usual.

E. Code Implementation and Execution Procedures

1. Extraction of Boundary-Layer Parameters

The computation of stability with the code Coast3 requires the local integral boundary-layer parameters and the local basic flow state. The boundary-layer edge is determined first. As the pressure can be assumed to be constant normal to the boundary layer, the boundary-layer edge velocity can be calculated from the wall pressure p_w using the Bernoulli equation:

$$U_e = \sqrt{U_\infty^2 - \frac{2\kappa}{\kappa - 1} \frac{p_\infty}{\rho_\infty} \left[\left(\frac{p_w}{p_\infty} \right)^{\frac{\kappa-1}{\kappa}} - 1 \right]}$$

Table 1 Tunnel data and experimental setup

	LNB	WUB	
Test section (width × height × length)	400 × 600 × 1200 mm	250 × 333 × 1250 mm	
Turbulence level	0.16%	0.8%	
Steady cases: angle of attack	4 deg	——	8 and 11 deg
Number of unsteady cases	——	case 1	case 2
Measurement window	9*27 × 22 mm	2*32 × 25 mm	41 × 15 mm
Focal length	105 mm	50 mm	120 mm
Interrogation window	16 × 16 px^2	32 × 32 px^2	16 × 16 px^2
Camera resolution	1280 × 1024	1280 × 1024	4008 × 2672
Spatial resolution	0.17 mm	0.39 mm	0.08 mm

Then, the boundary-layer thickness is found at the point in wall-normal direction where the total velocity exceeds a specified fraction $c \cdot U_e$ of the edge velocity, with $c = 0.99$ as a typical value. If this fraction is not obtained, then the point with the maximum velocity is taken instead. These criteria do not behave well in the region close to the leading stagnation point. Therefore, all points with a surface pressure coefficient of more than 95% of the stagnation value are excluded. This can be safely done because disturbances are damped in this region anyway.

The wall-tangential velocity component is then used to calculate boundary-layer parameters such as displacement thickness and momentum thickness. These boundary-layer parameters are transferred to Coast3 together with the velocity and temperature profiles (including their derivatives) from the URANS solution at each time step. Coast3 performs a cubic spline interpolation of the profiles and extracts a specified number of points from the splines. For all computations performed, a number of 50 points for the numerical solution of the stability equations was used.

2. N Factor for Stationary Flow

For the calculation of steady-state flows the linear stability solver is used in usual ways. First, the frequency range of amplified modes is estimated. Therefore, all eigenvalues at an initial station are searched. Then, the mode with the most amplified eigenvalue at this station is tracked up- and downstream until it is not amplified anymore. At these two positions, the modes with the highest and lowest frequency that are still amplified are determined. Second, an N factor analysis is performed in the previously determined frequency range for a number of fixed frequencies. For all these given frequencies, the most amplified modes are tracked up- and downstream until they are damped. Their temporal amplification rates are calculated in this region and transformed in spatial ones using the Gaster transformation. These are then integrated to N-factor distributions in the amplified region for every frequency. The envelope over all these N-factor distributions then yields the N-factor curve which is used to determine the transition location by comparison with a critical N factor.

3. N Factor for Unsteady Flow

The unsteady flow simulation uses the results from a preceding steady N-factor investigation as a start solution. That is, for every fixed frequency there exists locally one mode (the most amplified one) at the beginning. Multiple modes with different wave numbers and amplification rates may be found by the numerical method for a fixed frequency. All these modes are allowed for now, as a less amplified mode may become dominant during the unsteady computation. Accordingly, new amplified modes are searched after every time step at several positions on the airfoil within the range of the investigated frequencies. The amplitude exponent is now computed with the time-dependant scheme described in the preceding section for the maximum amplification factor at a given frequency. Numerically, this is achieved by specifying not only the frequency to investigate, but also using a mode wavelength and amplification rate from the last time step as initial value for the current time step. Additionally, as the frequency range of amplified

modes changes during the unsteady flow computation, the frequency range investigated is adapted during the computation.

4. Critical N Factor

The transition location is found by assuming a critical N factor at which breakdown to turbulence takes place and comparing it to the calculated N-factor distribution. For external flows in wind tunnels, the main factor influencing the critical N factor is the freestream turbulence level of the test section. An empirical correlation between the turbulence level and the critical N-factor N_{crit} given by Mack [28] was used to guide the values of the critical N factors of the present work.

$$N_{crit} = -8.43 - 2.4 \, \ell n (Tu) \qquad (1)$$

III. Flow Measurement Methods

A. Steady Onset Flow Conditions

Two-dimensional, phase-locked particle image velocimetry (PIV) measurements were conducted on the upper side of the SD7003 in the low turbulence wind tunnel (LNB) and the water tunnel (WUB) of the Technical University at Brunswick.[§] The wing section was made out of glass fiber reinforced epoxy with a chord length of 200 mm and a trailing-edge thickness of 0.3 mm. The measurements were carried out at a Reynolds number of $Re = 60$ K with the commercial PIV system FlowMaster 3S and a frequency doubled Quantel Twin double pulse Nd:YAG-laser. To achieve highly detailed measurements along the upper surface, the observation domain was translated to several positions, at which 1000 statistically independent PIV images were recorded to calculate the mean velocity and three components of the Reynolds stress tensor. For the evaluation of all images, the commercial PIV software DaVis 6.2 was used. Because of a high seeding density, it was possible to choose small interrogation windows. The specification of the tunnels and the experimental setup are summarized in Table 1. Note that the turbulence level for the wind tunnel has been measured by using hot wire anemometry, whereas PIV data with less resolution were used to measure the turbulence level of the water tunnel. In both tunnels, the full spectrum of fluctuations is assembled to obtain the turbulence level. PIV results for the low-Reynolds-number flow over the SD7003 airfoil obtained in various facilities including the LNB are compared and discussed by Ol et al. [29].

B. Flow for Airfoil with Hub Motion

Plunge motion of a two-dimensional airfoil in the water tunnel was obtained with a simple mechanical rig. The airfoil is attached to a linear track using axial ball bearings. The hydrodynamic forces at low Reynolds numbers and the inertial forces are small enough so that a one-sided attachment is sufficient, according to Fig. 1. Motion is generated by using an eccentric disc connected to an electric motor with a gear box. The device allows a plunge motion of ±25 mm with frequencies up to 2 Hz with 5% deviation estimated to the ideal sinusoidal stroke. Almost the same two-dimensional PIV setup was used as for the previously described water tunnel measurements. To

---
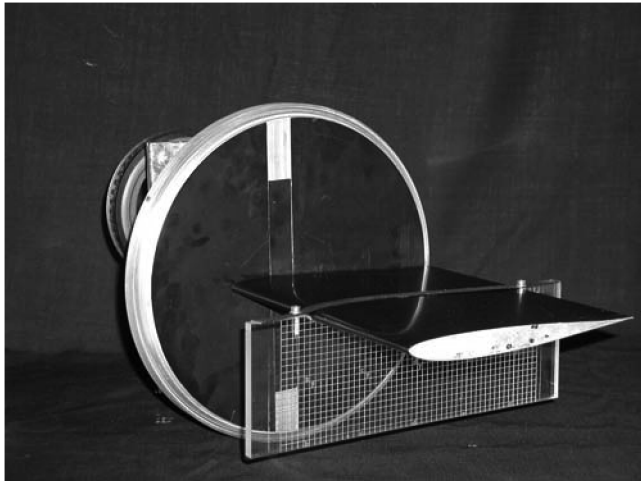
[§]www.tu-braunschweig.de/ism

Fig. 1 Plunge rig for two-dimensional airfoil motion in water tunnel (WUB).

cover most of the moving separation bubble, two slightly overlapping locations were chosen. Phase-averaged data are obtained by using a trigger signal that is generated by the motion apparatus. The trigger signal is used to trigger the sequencer card for synchronization of PIV laser and cameras.

IV. Results and Analysis

A. Verification of Numerical Simulations

The computational mesh for the numerical investigation of the SD7003 airfoil flow contains 1280×288 cells on the finest grid level, whereas most computations were performed on the second grid level with 640×144 cells. The grid is adapted to the expected flow features to have a good resolution of the LSBs over a range of incidence angles. Figure 2 shows the mesh on the fourth grid level in the vicinity of the airfoil. The far-field distance is 20 times the chord length.

The freestream Mach number was set to a value of 0.05 with low-speed preconditioning for all computations to simulate incompressible flow. Note that previous computations [16] indicated that this Mach number is low enough to exclude compressibility effects and there is no need to adapt the value to specific wind-tunnel or water-tunnel situations. For the large LSBs encountered at $Re = 60$ k without plunge motion of the airfoil, no converged results were obtained using the RANS solver in its steady mode. Therefore, all computations were performed in the time-accurate mode based on the dual time-stepping approach. The time step was chosen sufficiently small, resolving the time that the incoming flow would need to travel one chord length with 300 time steps. Steady-state solutions were found for high angles of attack, whereas periodic solutions were found at low angles of attack. In both cases, about 2000 time steps with about 20 inner iterations per time step were needed for the solution process. To stabilize the solution process, the transition location was predicted about every 10th time step. In these cases, the computational overhead for transition prediction module was about 5% using the 640×144 grid. For the low angles of attack where periodic solutions were obtained, the transition prediction was performed every time step for some cases, but no noteworthy oscillation in the transition location was found. Note that transition
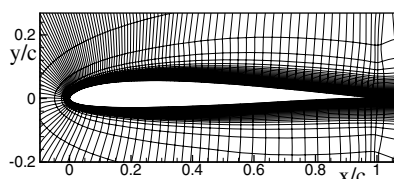

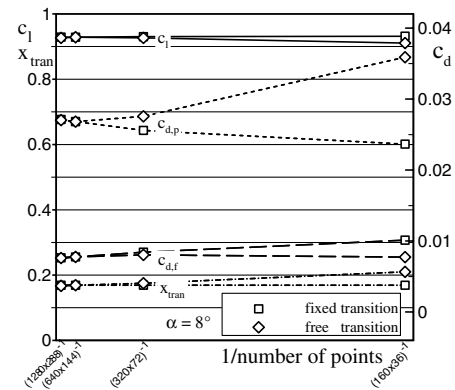Fig. 2 Computational mesh with 160×21 cells.

Fig. 3 Grid convergence of force coefficients using the Menter–BSL [34] model.
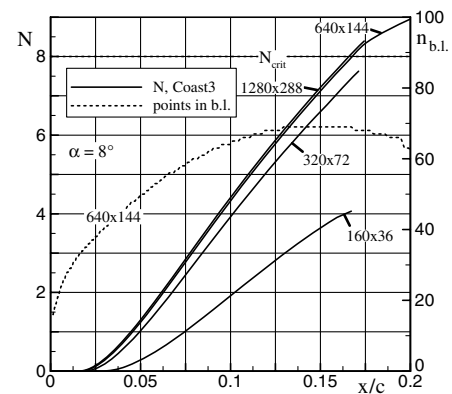

Fig. 4 Grid convergence of N-factor distribution for fixed transition location using the Menter–BSL [34] model.

prediction for these fully time-accurate solutions caused a CPU percentage of around 45%.

The influence of grid refinement on the force coefficients and the predicted transition location is shown in Fig. 3 for the angle of attack of $\alpha = 8$ deg. There, one set of computations was performed with free transition, whereas the other one was performed using the transition location found on the second grid level (640×144). A converged result is found on the grid with 644×144 cells. A similar study performed for $\alpha = 4$ deg yielded very similar results. The two sets of results illustrate that the large number of grid points used to achieve numerical errors of the drag value below 1% is due to the need to resolve both the laminar separation bubble and accurate N factors. The grid convergence of the N-factor distributions using the stability solver Coast3 is displayed in Fig. 4. The results are converged on the second grid level (640×144), whereas too low N factors are computed using numerical flow data of the RANS solver on the coarser meshes. This yields transition locations too much downstream, thereby increasing pressure drag and reducing friction drag on these meshes (see Fig. 3). Also shown in Fig. 4 is the number of grid points inside of the boundary layer for the grid with 644×144 cells. Here a number of about 50 points is inside of the boundary layer in the amplified region and this is generally sufficient for accurate N factors, according to our experience. Note that the amount of numerical dissipation was found to have no significant effect on the solutions for the finest and the second grid levels.

B. Analysis of Results for Steady-State Onset Flow

The analysis of numerically computed flows vs experimental data is complex because of the various models and assumptions involved. The present paper therefore reviews the experience gained with transition and turbulence models over the last years first. This status serves as a guideline to select a particular, promising combination of models that can be exploited for detailed comparisons with experimental data.
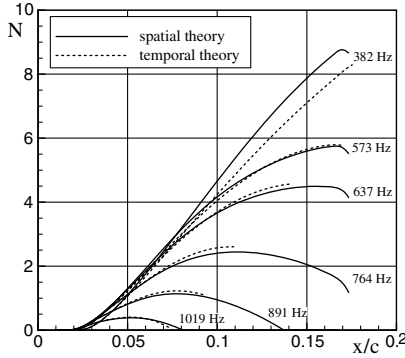
Fig. 5 Comparison of *N* factors in the laminar separation bubble of SD7003 airfoil in air, according to C. Atkin (from personal communications).

1. Fundamental Experience with Transition and Turbulence Models

Our numerical investigations use the computational setup as described in Sec. IV.A. In addition, LSBs at higher Reynolds numbers were also computed and compared with existing data. A variety of turbulence models has been investigated so far. The focus of interest was on the growth rate of turbulence within the transition region from laminar to fully turbulent shear layers and on the levels of shear stress around reattachment at the end of the bubble. Note again that laminar flow regions were simulated by switching off the production terms in the turbulence transport equations. It was found [17] that the onset and spreading of turbulence is much too strong using the local linear realizable model (LLR), linear explicit algebraic stress model (LEA) [30,31], and the 1988 and 1998 Wilcox k–ω models [32] which seems a behavior associated with the specific length scale equation. Growth of turbulence is too slow for the Spalart–Allmaras [33] and the Menter–SST models [34], on the other hand. A full Reynolds stress model composed of Speziale's pressure strain formulation [35] for turbulence away from walls and Wilcox's Reynolds stress model [32] close to walls devised by Eisfeld [23] performed well at higher Reynolds numbers but it yielded too low levels of Reynolds stresses for low Reynolds numbers [36]. Good overall results were obtained for the Menter baseline model [34] termed BSL k–ω model, and the Wallin explicit algebraic stress model [37]. This concerns comparisons with measured PIV data and well resolved LES [17]. Therefore, only the results for these turbulence models are presented next.

Fundamental experience was also gained by using a variety of transition models along with the e^N method as described before. In particular, the results for the N factor as computed by the stability solver Coast3 were compared with approximate envelope methods taken from the two-dimensional airfoil code XFOIL [15]. In general, both approaches yield rather similar values of N, and the envelope can be used for steady-flow cases within the parameter range investigated here. However, there seems no straightforward way to extend the approximate envelope approach to genuinely unsteady boundary layers.

The validity of Gaster's transformation between temporal and spatial growth rates is also investigated. Figure 5 displays computed N factors by using temporal theory and spatial theory for the SD7003 airfoil at 8 deg angle of attack, where a laminar separation bubble exists at $0.05 < x/c < 0.20$. It is seen that the computed N factors compare very well, even across the laminar separation. It is only toward the end of the transition region that some noticeable differences occur, and these are below one for the value of N.

2. Validation Results of Flowfield Investigations

The focus of interest in validation is on the growth rate of turbulence within the transition region from laminar to fully turbulent shear layers and on the levels of shear stress around reattachment at the end of the bubble. The turbulent shear stress, $\tau_{xy} = -\rho \overline{u'v'}$, causes transport of momentum across the boundary layer, which is responsible for the closure of the LSB. For the present URANS
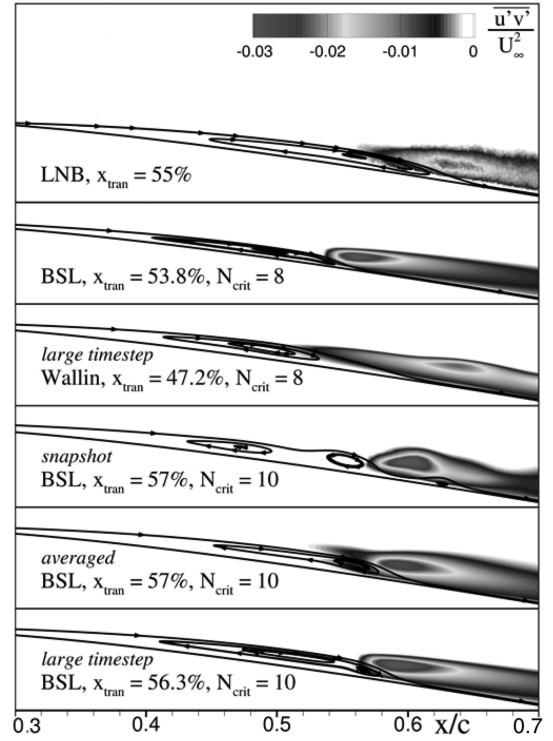

Fig. 6 Experimental and numerical streamlines and turbulent shear stress for $\alpha = 4 \deg$.

results using eddy-viscosity models, $\overline{u'v'}$ was recovered based on the Boussinesq approximation:

$$\overline{u'v'} = -\frac{\mu_t}{\rho}\left(\frac{\partial \tilde{u}}{\partial y} + \frac{\partial \tilde{v}}{\partial x}\right) + (\overline{uv} - \bar{u}\,\bar{v}) \qquad (2)$$

where $\tilde{u}$ and $\bar{u}$ denote the ensemble-averaged and time-averaged mean values, respectively. The second part of Eq. (2) is used to take into account the mean-flow oscillations that are encountered in some of the calculations in the form of shed vortices. This account is necessary because the shedding of vortices that occurs in the experiment contributes to the measured shear stress as well. Note that Eq. (1) is an approximation for unsteady flows as not all velocity correlations for a full account of $\overline{u'v'}$ are given by the RANS solution. For steady LSBs found at higher angles of attack, the latter part of Eq. (2) diminishes and $\tilde{u} = \bar{u}$.

The transition location in the measurements is defined as the beginning of the turbulent wedge that spreads from the shear layer of the LSB. In particular, the point is taken where the normalized Reynolds shear stress obtains 0.1% and demonstrates a clearly visible rise. Otherwise, measurement errors due to insufficient resolution of the flapping of the laminar part of the LSB could be misinterpreted as turbulent flow.

The measured and computed LSBs and the corresponding shear stress distributions for an angle of attack of 4 deg are displayed in Fig. 6. The experimental data were taken in the low-disturbance wind tunnel (LNB), and therefore rather large values of the critical N factor seem appropriate. Note that very similar experimental results were obtained by Ol et al. [29] in two water facilities. Simulations with Menter's BSL model and $N_{\text{crit}} = 8$ exhibit a somewhat too strong onset of turbulence, which results in a rapid closure of the bubble. Therefore, the bubble becomes rather thin with results in lower amplification rates and thus transition location is downstream of the measured one. Temporal fluctuations of the LSB were resolved using the Wallin [37] model at $N_{\text{crit}} = 8$, and for both models at $N_{\text{crit}} = 10$. This is shown as a snapshot for the Menter–BSL model and $N_{\text{crit}} = 10$. Inspection of the temporal development of the numerical solution indicates that the fluctuations originate from an instability in the laminar part of the LSB. To see if this behavior has a noteworthy
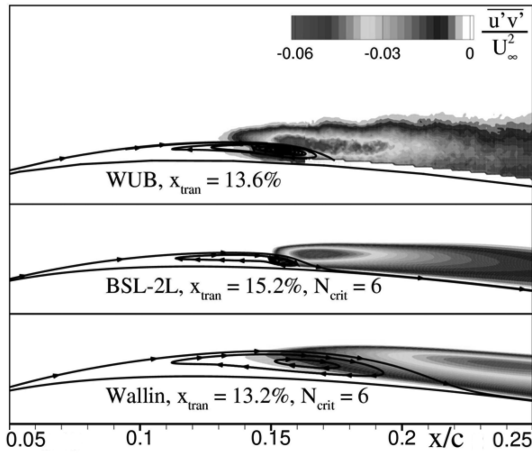
Fig. 7   Experimental and numerical streamlines and turbulent shear stress for $\alpha = 8\,\mathrm{deg}$.

Fig. 8   Experimental and numerical streamlines and turbulent shear stress for $\alpha = 11\,\mathrm{deg}$.

effect on the numerical solution, additional runs were performed using a larger time step that did not resolve the instability. These yielded steady-state solutions with only minor differences to the time-averaged result; see bottom of Fig. 6. The comparison of the numerical simulations and experimental data given in Fig. 6 indicates that a critical N factor of $N_{\mathrm{crit}} = 10$ seems appropriate for simulating LNB flows.

The numerically resolved oscillations appear as vortex shedding. A single period of this process is typically resolved by using about 50 time steps, and the computed shedding frequency is found to be $f = 125\,\mathrm{Hz}$ in air. Coast3 predicts the most amplified frequencies in a range of about $120 < f < 170\,\mathrm{Hz}$, based on linear stability assumptions. Converted to the flow conditions of the water tunnel, WUB, the computed shedding frequency becomes $f_{\mathrm{water}} = 8.5\,\mathrm{Hz}$. This agrees reasonably well with recent measurements performed in the WUB, where two-dimensional waves were captured using time-resolved PIV [38] and had a frequency of $f = 12\,\mathrm{Hz}$. Both the good agreement with Coast3 as well as with the measurement lead to the conclusion that a KH instability of the LSB is resolved in the RANS computation for $\alpha = 4\,\mathrm{deg}$.

The computational and experimental results for the 8 deg case are shown in Fig. 7. Onset of turbulence and the bubble vortex core in the measurement are located only slightly upstream compared with the calculations using the BSL model. As $N_{\mathrm{crit}} = 6$ was used for the calculations, it seems that the empirical correlation of Eq. (1) based on the nominal turbulence in the WUB water tunnel would yield a too low value of $N_{\mathrm{crit}} = 3.0$. Note that the resulting LSB for $N_{\mathrm{crit}} = 3.0$ would be much too short (not shown here). As for the 4 deg case, the onset of turbulence appears too rapid for the BSL model. The minimum values of $\overline{u'v'}$ in the measurements agree well with computation.

To improve the performance of the BSL model at higher angles of attack, it was used in a so called two-layer mode (BSL-2L), as proposed by Menter [34]. With this variant, the blending from the ω length scale equation that is used close to the wall to the ε equation in the outer boundary-layer region is located closer to the wall. This yields a later onset of turbulent flow separation. Up to angles of attack of about 8 deg, no noteworthy difference is found between the two variants of the BSL model. For the Wallin model, the onset of turbulence is too slow for the higher angles of attack. This leads to a too thick and long bubble.

The angle of attack, $\alpha = 11\,\mathrm{deg}$, is close to maximum lift making this case very challenging to simulate. The BSL model gives a trailing-edge separation starting at $\alpha = 10\,\mathrm{deg}$, whereas the flow in the WUB is still attached for 11 deg. The trailing-edge stall is suppressed for the BSL-2L variant. Using $N_{\mathrm{crit}} = 7$ rather than $N_{\mathrm{crit}} = 6$, the resulting LSB matches the measurement very well regarding the shape, transition location, and distribution, as well as minimum value of $\overline{u'v'}$, as seen in Fig. 8. For the Wallin model, as for the 8 deg case, the onset of turbulence is too slow, resulting in a
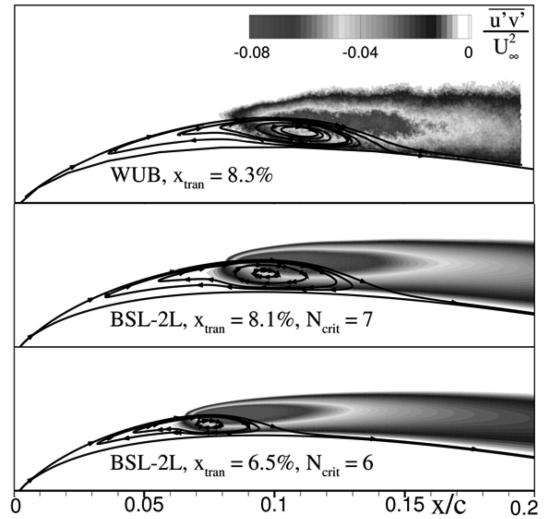
bubble with a length of almost half of the airfoil (not shown). Concluding our results for the N factor we find that a critical value in the range of 6–7 is appropriate for the water tunnel WUB facility.

3.   Lift and Drag Coefficients

The computed force coefficients are compared with the measured data by Selig et al. [4,5] in Fig. 9. It is noticeable that the measurements in the tunnels at Illinois and Princeton give rather different results even though both test sections and models had approximately the same size, about the same turbulence level, and appropriate wall corrections were applied. For the low-Reynolds number of $Re = 60\,\mathrm{k}$, it was found in the Illinois measurement that the wake flow was not two-dimensional, resulting in a strong influence of the spanwise measurement position on the drag coefficient. During the Illinois measurements, endplates were used to isolate the ends of the model from the tunnel sidewall boundary layers.

Given the uncertainty in the measured coefficients, the calculated values agree very well. For the low angles of attack, although LSBs with different sizes were calculated for the applied turbulence models, the computed drag coefficients differ only slightly. Obviously, the contribution of an elevated pressure drag for a larger bubble is compensated by a reduced friction drag due to the larger and stronger recirculation area. For the higher angles of attack, the pressure drag becomes dominant and the bubble size is more important. The Wallin model gives significantly higher drag than the BSL models, at larger angles of attack. For further increased angles, the BSL-2L variant yields the largest lift coefficients because trailing-edge stall occurs later.

The force coefficients for the BSL-2L model are compared with the results of XFOIL in Fig. 10 for various critical N factors. The drag
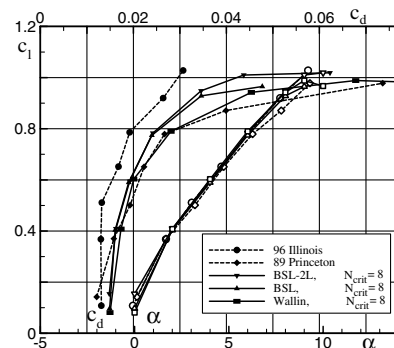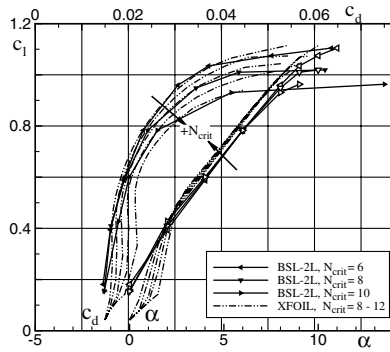

Fig. 9   Computed and measured force coefficients.

Fig. 10 Effect of N_{crit} on computed force coefficients and comparison with two-dimensional airfoil code XFOIL.
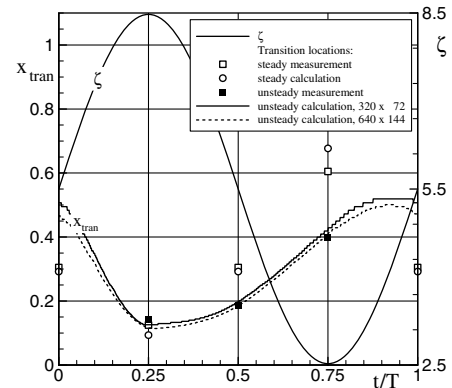

Fig. 11 Effective angle of attack and transition locations along airfoil surface for unsteady case 1.

Fig. 12 Computed force coefficients for unsteady case 1.

polars agree very well for the high angles of attack. Higher critical N factors are generally needed for XFOIL to match the FLOWer results because of XFOIL's thinner LSBs. In particular, N_{crit} has to be increased by about $\Delta N = 2$. For the lower angles of attack, the FLOWer results show little influence on the critical N factor applied. As explained before, this is because an increased pressure drag is compensated by a reduced friction drag. In contrast, XFOIL gives a rather constant friction drag for angles of attack of $\alpha \leq 2$ deg, whereas the pressure drag is also increased due to larger LSBs at higher N_{crit}. Unfortunately, no measurement data are available that can be used for validation at the low angles of attack. For $\alpha = 0$ deg, the FLOWer calculations for $N_{crit} \geq 8$ and all XFOIL calculations predict a fully laminar flow, which is why the results do not vary with N_{crit}.

C. Analysis of results for airfoil with plunge motion

Computational results for the SD7003 airfoil with plunging motion are obtained along with the measurements conducted in the water tunnel. Two sets of motion parameters are investigated, both at a Reynolds number of 60 k. The first experiment denoted with case 1 is designed to yield continuous movement of transition location along the airfoil surface. The mean angle of attack is defined as $\alpha_0 = 5.5$ deg. With $U_\infty = 0.3$ m/s, a flapping frequency of $f = 0.25$ Hz, and a plunging amplitude of $z_1 = 10$ mm, the resulting quasi-steady equivalent angle-of-attack amplitude from plunging is calculated as $\zeta_1 = 2\pi f z_1/U_\infty = 3$ deg. The resulting effective angle of attack for the airfoil motion then reads $\zeta = \alpha_0 + \zeta_1 \sin(2\pi ft) = 5.5$ deg $+3$ deg $\sin(2\pi ft)$ and $k = \pi ft/U_\infty = 0.52$. Phase-locked measurements were performed for the four motion positions top dead center (TDC) ($\zeta = 5.5$ deg), down stroke ($\zeta = 8.5$ deg), bottom dead center (BDC) ($\zeta = 5.5$ deg), and upstroke ($\zeta = 2.5$ deg). Additional measurements were carried out for these four angles of attack for steady onset conditions.

The numerical results were obtained using the e^N method with the extension for unsteady flows as described in Sec. II. The critical N factor was set to $N_{crit} = 6$. Note that the N-factor distribution of the unsteady scheme yields identical values for cases with steady onset conditions as both are based on the same solver for the temporal stability problem. As the BSL-2L turbulence model showed a rather good performance for the steady onset condition calculations, it was chosen for the unsteady calculation as well. To take into account the wall effect from the water-tunnel experiment, a simple wall correction for steady flows [39] was applied. This results in an effective angle of attack of $\zeta = 6$ deg $+3.3$ deg $\sin(2\pi ft)$ which was used for the calculations. This was accomplished with a reduced frequency of $k = 0.52$ and a plunge amplitude of $z_1/c = 0.0554$.

Figures 11 and 12 display the temporal distributions of transition location and force coefficients. The experimental transition locations for these phase-locked measurements were determined similarly to the measurement at steady onset conditions, as described earlier. Care was taken to ensure that fully periodic numerical solutions were obtained by running three motion periods in total. Time accuracy of the numerical solution was checked by halving time steps. The results for the 320×72 and 640×144 meshes indicate that grid
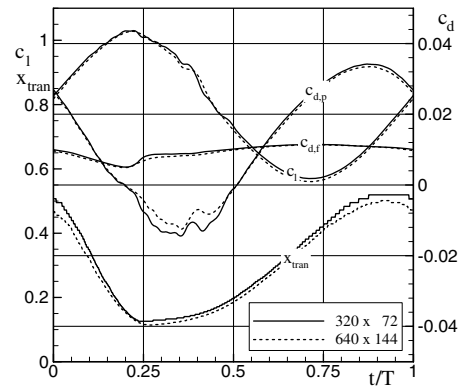
convergence to engineering accuracy is obtained. The data for steady-state onflow with equivalent angles of attack are also included. Some discrepancies between computed and measured transition location are observed for steady flow at the lowest angle of attack, most probably caused by the tendency of the BSL-2L model to yield too thin bubbles. In the unsteady computation, it was observed that the frequencies of the most amplified two-dimensional, boundary-layer modes were at least 30 times larger than the frequency of airfoil motion, in agreement with the assumptions of Sec. II.C. A strong effect of unsteady boundary-layer flow on transition is seen in that the unsteady transition locations are downstream of the steady ones at $\zeta = 8.5$ deg, whereas it is the other way around at the lower angles. For this effect, very good agreement between measurement and calculation is found which indicates that the unsteady transition model is well formulated. The physical explanation of the effect is that the boundary layers at small ζ values have experienced large effective angles during previous phases, with stronger adverse pressure gradients and the corresponding destabilizing effects on unstable modes. Opposite effects are introduced at large ζ values. The computed unsteady transition location shows a phase lag of around 10 deg during the downstroke and 60 deg during upstroke. The lift coefficient, however, displays a negative phase shift of around -20 deg which is caused by the positive phase lag of viscous momentum losses in the boundary layer.

The measured and computed LSBs are finally compared at the dead centers, downstroke and upstroke in Fig. 13, together with contour levels of the shear stress $\overline{u'v'}$. To draw streamlines, the v component of the velocity is corrected with the plunging velocity of the airfoil, leading to a velocity of zero on the surface of the airfoil. The experiments display local regions with elevated shear stress which indicates that the periodic shedding of vortices behind the LSB is coupled to the plunge motion, which has a much lower frequency. This is explained by the delayed transition at large ζ values as seen in Fig. 11, which may trigger the shedding of a vortex. Further, despite
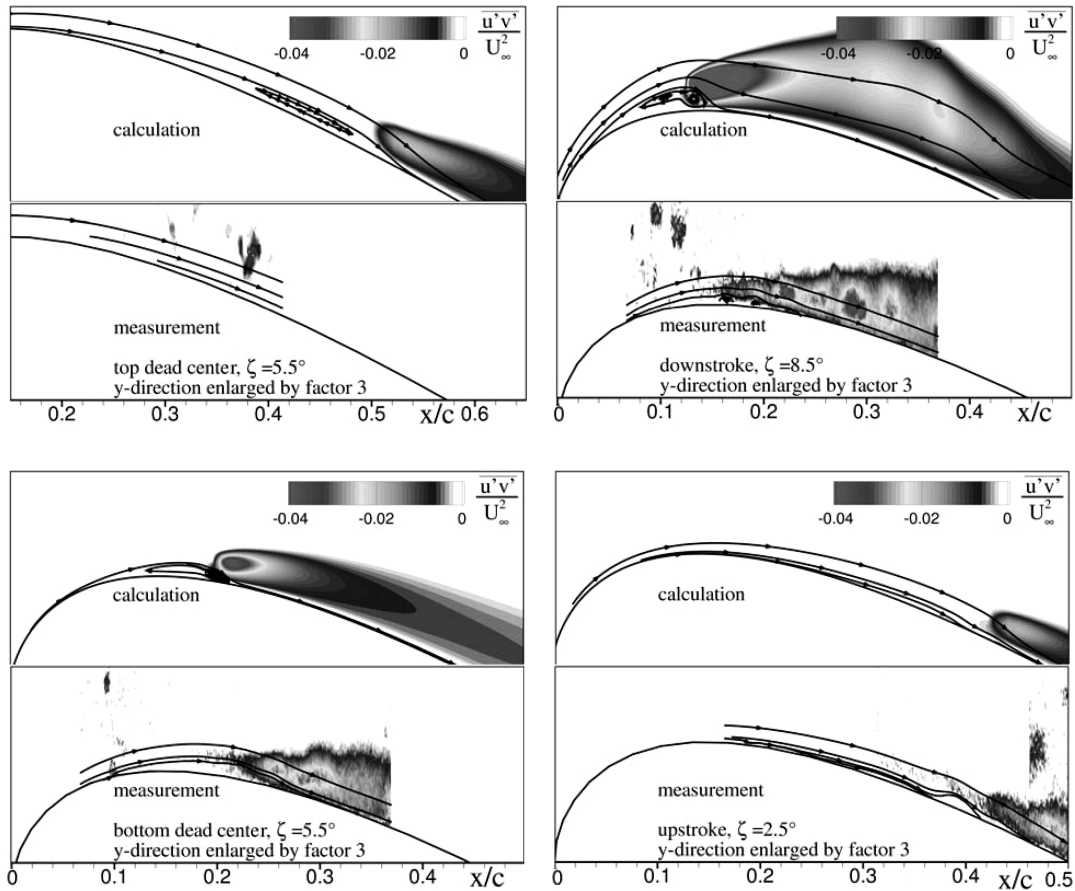
Fig. 13 Comparison of streamlines and turbulent shear stress at four phase angles for case 1, grid 640 × 144.

the same quasi-steady angle of attack of $\zeta = 5.5$ deg, there are completely different flow states found at TDC and BDC. Although the LSB that forms during the downstroke is clearly visible at BDC, it is rather small during upstroke and at TDC. A transition location cannot be determined in the measurement window for TDC.

The second experiment denoted with case 2 is designed to yield a strong variation of transition location. The mean angle of attack is defined as $\alpha_0 = 4.0$ deg. The quasi-steady equivalent angle-of-attack amplitude from plunging is $\zeta_1 = 4.6$ deg. The resulting effective angle of attack for the airfoil motion then reads $\zeta = 4.0$ deg $+ 4.6$ deg $\sin(2\pi f t)$ and $k = \pi f t / U_\infty = 0.8$. Phase-locked measurements were performed for the four motion positions top dead center ($\zeta = 4.0$ deg), downstroke ($\zeta = 8.6$ deg), bottom dead center ($\zeta = 4.0$ deg), and upstroke ($\zeta = -0.6$ deg). Additional measurements were carried out for steady onset conditions. Again, wall corrections for steady flows [39] were applied to the numerical

computations. This results in an effective angle of attack of $\zeta = 4.3$ deg $+4.9$ deg $\sin(2\pi f t)$ used for the calculations.

Figures 14 and 15 display the temporal distributions of transition location and force coefficients for case 2. The numerical solutions are periodic. Some discrepancies between computed and measured transition location are observed in that transition is computed somewhat downstream of the measured values. The effect of unsteady boundary-layer flow on transition is stronger than for case 1. Again, good agreement between measurement and calculation is found both for the change of transition location and its phase lag. The computed lift and drag coefficients are strongly affected by the variations of transition as large laminar separations occur around $t/T = 0.25$. At this point in the motion, period turbulent shear stresses are low and develop slowly even though transition location is around $x/c = 0.30$.

The measured and computed flowfields are compared at the dead centers, downstroke, and upstroke in Fig. 16. The results display
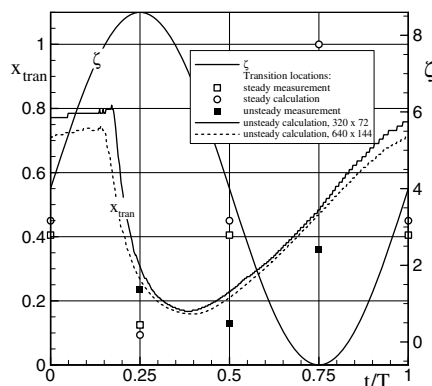

Fig. 14 Effective angle of attack and transition locations along airfoil surface for unsteady case 2.
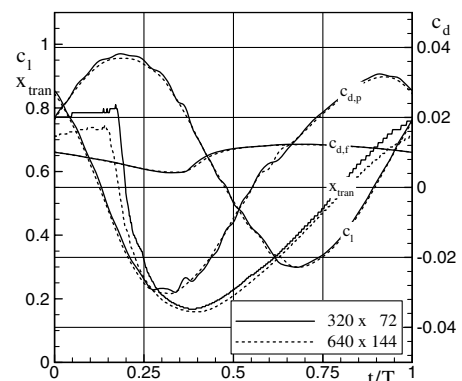

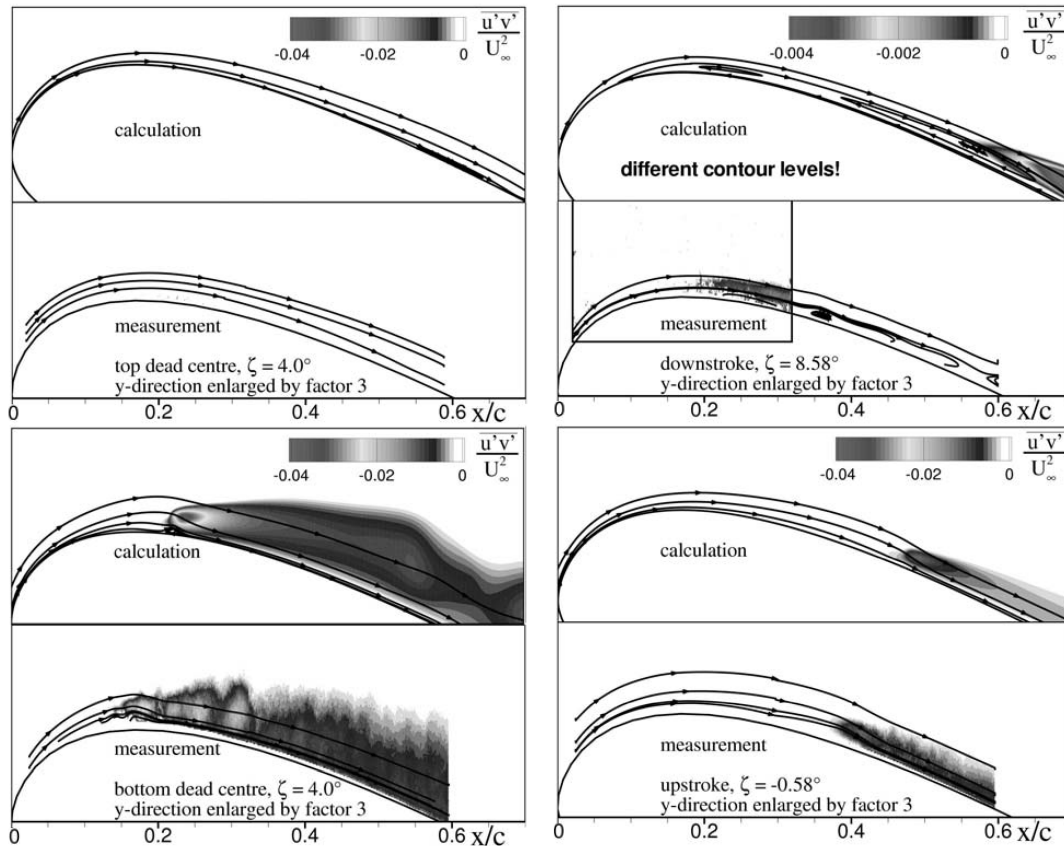Fig. 15 Computed force coefficients for unsteady case 2.

Fig. 16 Comparison of streamlines and turbulent shear stress at four phase angles for case 2, grid 640 × 144.

large regions with laminar flow at TDC. Low levels of turbulence are visible at the downstroke position, as transition to turbulence has just taken place (see Fig. 14). The flow exhibits multiple laminar flow separations. At BDC the thick boundary-layer flow along the upper surface is strongly turbulent, as the result of the preceding flow separations, and there is almost no flow separation visible.

V. Conclusions

Experimental measurements and unsteady RANS simulations of the low-Reynolds-number flow past an SD7003 airfoil with and without plunge motion at $Re = 60$ k were conducted. Laminar separation bubbles are present and they are an important phenomenon of this flow regime. The experimental data consist of high-resolution, phase-locked PIV measurements in a wind tunnel and a water tunnel. The numerical simulation approach includes transition prediction which is based on linear stability analysis applied to unsteady mean-flow data. The numerical results obtained for steady onflow are validated against PIV data and published force measurements. Good agreement is obtained for Menter's baseline turbulence model. Flows with plunge motion reveal strong effects of flow unsteadiness on transition and the resulting flowfields with laminar separation bubbles. The unsteady flow effects are very well captured in the simulation. This indicates that the novel formulation of the unsteady transition model is physically sound.

The results demonstrate that transition and turbulence play an important role in the unsteady aerodynamics of flapping airfoils and wings at the Reynolds numbers of birds and micro aerial vehicles and should be taken into account during design and optimization.

Acknowledgments

References

[1] Schmitz, F. W., *Aerodynamik des Fluges*, Verlag Carl Lange, Duisburg, Germany, 1960.

[2] Eppler, R., *Airfoil Design and Data*, Springer–Verlag, Berlin, ISBN 3-540-52505-X, 1990.

[3] Althaus, D., *Profilpolaren für den Modellflug*, Vol. 1, ISBN 3-7883-0158-9; Vol. 2, ISBN 3-7883-0134-1, Neckar–Verlag, Villingen-Schwenningen, Germany, 1985.

[4] Selig, M. S., Donovan, J. F., and Fraser, D. B., *Airfoils at Low Speeds*, edited by H. A. Stokely, Soartech Aero Publications, Virginia Beach, VA, 1989.

[5] Selig, M. S., Guglielmo, J. J., Broeren A. P., Giguere, P., Lyon, C. A., Ninham, C. P., and Gopalarathnam, A., *Summary of Low-Speed Airfoil Data*, (edited by) H. A. Stokely, SoarTech Aero Publications, Virginia Beach, VA, Vols. 1–3, 1995–1997.

[6] Send, W., "Otto Lilienthal und der Mechanismus des Schwingenflugs," *DGLR Jahrbuch 1996*, Vol. 1, Deutsche Gesellschaft fuer Luft und Raumfahrt–Lilienthal–Oberth, Bonn, Germany, 1996, pp. 161–172.

[7] Jones, K. D., Lund, T. C., and Platzer, M. F., "Experimental and Computational Investigation of Flapping-Wing Propulsion for Micro-Air Vehicles," *Progress in Astronautics and Aeronautics Series*, (edited by) T. J. Mueller, AIAA, Reston VA, Chap. 16, 2002, pp. 307–339.

[8] Neef, M. F., "Analyse des Schlagflugs Durch Numerische Strömungsberechnung," Ph.D. Thesis, Technical Univ. of Brunswick, ZLR Forschungsbericht 2002-02, 2002; www.biblio.tu-bs.de/ediss/data/20021021a/20021021a.html.

[9] Tuncer, I. H., and Kaya, M., "Optimization of Flapping Airfoils for Maximum Thrust and Propulsive Efficiency," *AIAA Journal*, Vol. 43, No. 11, 2005, pp. 2329–2336.

[10] Grasmeyer, J. M., and Keennon, M. T., "Development of the Black Widow Micro Air Vehicle," AIAA Paper 2001-0127, 2001.

[11] Würz, W., "Hitzdrahtmessungen zum laminar-turbulenten Strömungsumschlag in anliegenden Grenzschichten und Ablöseblasen sowie Vergleich mit der laminaren Stabilitätstheorie und empirischen Umschlagskriterien," Ph.D. Thesis, Univ. Stuttgart, Germany, 1995.

[12] Lang, M., Marxen, O., Rist, U., and Wagner, S., *Experimental and Numerical Investigations on Transition in a Laminar Separation Bubble*, edited by Wagner, S., Rist, U., Heinemann, H. J., and Hilbig, R., Notes on Numerical Fluid Mechanics and Multidisciplinary Design, Vol. 77, Vieweg, Brunswick, Germany, 2002, pp. 207–214.

[13] Marxen, O., Rist, U., and Wagner, S., "Effect of Spanwise-Modulated Disturbances on Transition in a 2-D Separated Boundary Layer," AIAA Paper 2003-0789, 2003.

[14] Rist, U., "Instability and Transition Mechanisms in Laminar Separation Bubbles," *Low Reynolds Number Aerodynamics on Aircraft*, Proceedings of Von Karman Institute Lecture Series, RTO-AVT-VKI-104, Research and Technology Agency—Applied Vehicle Technology, Neuilly sur Seine, France, 2005.

[15] Drela, M., "XFOIL: An Analysis and Design System for Low Reynolds Number Airfoils," *Low Reynolds Number Aerodynamics*, edited by T. J. Mueller, Lecture Notes in Engineering, Springer–Verlag, New York, 1989.

[16] Windte, J., Scholz, U., and Radespiel, R., "Validation of the RANS-Simulation of Laminar Separation Bubbles on Airfoils," *Aerospace Science and Technology*, Vol. 10, No. 6, 2006, pp. 484–494.

[17] Yuan, W., Khalid, M., Windte, J., Scholz, U., and Radespiel, R., "Computational and Experimental Investigation of Low-Reynolds-Number Flows past an Airfoil," AIAA Paper 2005-4607, 2005.

[18] Watmuff, J. H., "Evolution of a Wave Packet into Vortex Loops in a Laminar Separation Bubble," *Journal of Fluid Mechanics*, Vol. 397, Oct. 1999, pp. 119–169.

[19] Van Ingen, J. L., "Suggested Semi-Empirical Method for the Calculation of the Boundary Layer Transition Region," Dept. of Aerospace Engineering, Rept. VTH-74, Delft Univ. of Technology, 1956.

[20] Stock, H. W., and Haase, W., "Feasibility Study of e^N Transition Prediction in Navier–Stokes Methods for Airfoils," *AIAA Journal*, Vol. 37, No. 10, 1999, pp. 1187–1196.

[21] Stock, H. W., and Haase, W., "Navier-Stokes Airfoil Computations with the e^N Transition Prediction Including Transitional Flow Regions," *AIAA Journal*, Vol. 38, No. 11, 2000, pp. 2059–2066.

[22] Kroll, N., Rossow, C. C., Schwamborn, D., Becker, K., and Heller, G., "MEGAFLOW: A Numerical Flow Simulation Tool for Transport Aircraft Design," International Council of the Aeronautical Sciences Paper No. 1105, Toronto, 2002.

[23] Eisfeld, B., "Numerical Simulation of Aerodynamic Problems with Reynolds Stress Turbulence Models," *14th STAB Symposium, Bremen, Germany, 16–18 Nov. 2004*, Notes on Numerical Fluid Mechanics and Multidisciplinary Design, Vol. 92, Springer–Verlag, Berlin, 2006.

[24] Schrauf, G., "Coast3: A Compressible Stability Code. User's Guide and Tutorial," Daimler–Benz Aerospace Airbus, TR EF 040/98, Bremen, Germany, 1998.

[25] Schrauf, G., "Algorithm 696: Inverse Rayleigh Iteration for Complex Band Matrices," *ACM Transactions on Mathematical Software*, Vol. 17, No. 3, 1991, pp. 335–340.

[26] Schrauf, G., "Transition Prediction Using Different Linear Stability Analysis Strategies," AIAA Paper 94-1848-CP, 1994.

[27] Gaster, M., "Relation Between Temporally Increasing and Spatially Increasing Disturbances in Hydrodynamic Stability," *Journal of Fluid Mechanics*, Vol. 14, Part 2, Oct. 1962, pp. 222–224.

[28] Mack, L. M., "Transition and Laminar Instability," *Jet Propulsion Laboratory Publication 77-15*, Jet Propulsion Lab., Pasadena, CA, 1977.

[29] Ol, M., McAuliffe, B. R., Hanff, E. S., Scholz, U., and Kaehler, C., "Comparison of Laminar Separation Bubble Measurements on a Low Reynolds Number Airfoil in Three Facilities," AIAA Paper 2005-5149, 2005.

[30] Rung, T., and Thiele, F., "Computational Modeling of Complex Boundary-Layer Flows," *Proceedings of the 9th International Symposium on Transport Phenomena in Thermal-Fluid Engineering, Singapore*, Pacific Center of Thermal Fluids Engineering, Kihei, HI, 1996.

[31] Rung, T., Lübcke, H., Franke, M., Xue, L., Thiele, F., and Fu, S., "Assessment of Explicit Algebraic Stress Models in Transonic Flows," *Engineering Turbulence Modeling and Experiments 4*, edited by W. Rodi and D. Laurence, Elsevier, Amsterdam, 1999, pp. 659–668.

[32] Wilcox, D. C., *Turbulence Modeling for CFD*, DCW Industries, La Cañada, CA, 1998.

[33] Spalart, P. R., and Allmaras, S. R., "One-Equation Model for Aerodynamic Flows," AIAA Paper 92-439, 1992.

[34] Menter, F. R., "Two-Equation Eddy-Viscosity Transport Turbulence Model for Engineering Applications," *AIAA Journal*, Vol. 32, No. 8, 1994, pp. 1598–1605.

[35] Speziale, C. G., Sarkar, T. B., and Gatski, T. B., "Modelling the Pressure-Strain Correlation of Turbulence: An Invariant Dynamical Systems Approach," *Journal of Fluid Mechanics*, Vol. 227, June 1991, pp. 245–272.

[36] Windte, J., and Radespiel, R., "RANS Simulation of the Transitional Flow Around Airfoils at Low Reynolds Numbers for Steady and Unsteady Onset Conditions," *Proceedings of Specialists Meeting on Enhancement of NATO Military Flight Vehicle Performance by Management of Interacting Boundary Layer Transition and Separation, Prague, Czech Republic*, Research and Technology Agency–Applied Vehicle Technology, Neuilly sur Seine, France, RTO-MP-AVT-111-P-03, 2004.

[37] Wallin, S., and Johansson, A., "Explicit Algebraic Reynolds Stress Model for Incompressible and Compressible Turbulent Flows," *Journal of Fluid Mechanics*, Vol. 403, Jan. 2000, pp. 89–132.

[38] Hain, R., and Kaehler, C. J., "Advanced Evaluation of Time-Resolved PIV Image Sequences," *6th International Symposium on Particle Image Velocimetry*, California Inst. of Technology, Pasadena, CA, 2005.

[39] Ewald, B. F. R. (Ed.), "Wind Tunnel Wall Corrections," AGARD AG-336, ISBN 92-836-1076-8, 1998, pp. 2–14.

Z. Wang
Associate Editor